Chapter 4

Launcher Aerodynamics: A Suitable Investigation Approach at Phase-A Design Level

Giuseppe Pezzella and Antonio Viviani

Additional information is available at the end of the chapter

http://dx.doi.org/10.5772/intechopen.70757

Abstract

This chapter deals with launcher aerodynamic design activities at phase-A level. The goal is to address the preliminary aerodynamic database of a typical launch vehicle configuration as input for launcher performances evaluations, control, sizing, and staging design activities. In this framework, different design approaches relying on both engineering and numerical methods are considered. Indeed, engineering-based aerodynamic analyses by means of a three-dimensional panel methods code, based on local surface inclination theory, were performed. Then, accuracy of design analysis increased using steady-state computational fluid dynamics with both Euler and Navier-Stokes approximations.

Keywords: launcher vehicles, aerodynamic design, subsonic, transonic, supersonic and hypersonic speed flows, computational fluid dynamics, panel methods aerodynamics

1. Introduction

During the design phase of launchers, the aerodynamic characterization represents a fundamental contribution. Usually, it is accomplished by means a hybrid approach encompassing wind tunnel testing (WTT) and computational fluid dynamics (CFD) investigations [1]. This combined design approach (i.e., WTT and CFD analyses) is extremely reliable in providing high quality data as input for launchers' sizing, performance evaluations, control, and staging dynamics [2]. Indeed, launcher aerodynamics focuses on the assessment of the pressure and skin friction loads the atmosphere determines over the vehicle surface [3]. As well known, these loads result in a global aerodynamic force that acts at the aeroshape center of pressure (CoP) which generally does not coincide with the vehicle center of gravity (CoG) [4]. As a result, the related aerodynamic moment acting at the CoG can lead to a stable or unstable behavior of the launcher to account for in the control software [5]. Moreover, the analysis of the flowfield past the launcher is also fundamental to address the effects of aeroshape's structures

and protrusions. Indeed, aeroshell steps and gaps determine local pressure (and convective heat flux) overshoots all along the ascent trajectory [6]. This assessment is fundamental for launcher sizing and thermal protection design activities [7].

With this in mind, the present research effort describes typical aerodynamic analyses performed at Phase-A design level [8]. Indeed, engineering-based analyses are carried out by exploiting local surface inclinations methods. After that, fully three-dimensional steady-state CFD analyses have been addressed to feed launcher aerodynamic design in the range between Mach 0.5 and 5.

Nevertheless, this chapter opens focusing attention on the assessment of the reliability of the present numerical design approach. Indeed, a CFD validation study was undertaken in order to highlight the capability of this CFD approach in assessing some critical aerothermal design issues, namely shock-shock interaction (SSI) and shock wave boundary layer interaction (SWIBLI), of vehicle aeroshapes flying at hypersonic speed, like launchers.

Finally, note that numerical flowfield analyses are performed with FLUENT code and perfect gas flow model.

2. CFD validation study

In the last years, CFD has played an important role in hypersonics being able to address particular design issues, such as the well-known SSI and SWIBLI [4]. These flowfield features occur whenever different shocks interact each other or with the boundary layer when a shock impinges on a wall, respectively. For launchers, SSI and SWIBLI phenomena typically take place in the flowfield region within launcher main body and boosters, as shown in the schematics of **Figure 1**.

In this figure, the fairings bow shock meets that of booster, thus originating a SSI. This interaction results in more or less complex shock patterns including shear-layers or jets, which

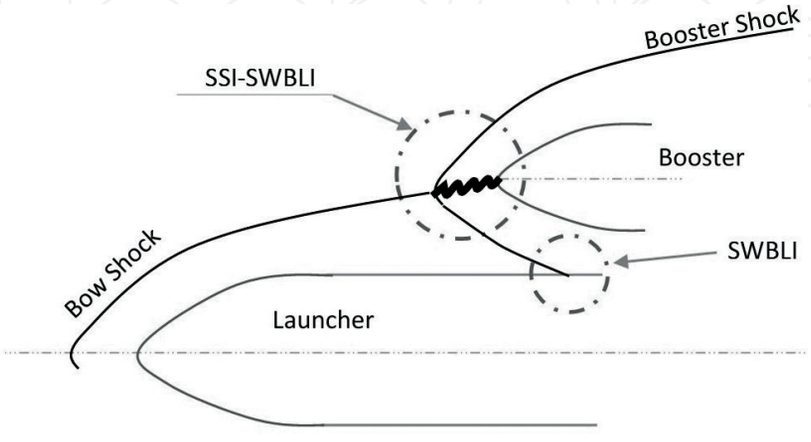

Figure 1. Example of SSI and SWBLI for launchers.

http://dx.doi.org/10.5772/intechopen.70757

can impinge on the launcher aeroshape and cause local pressure and heat flux overshoots, well in excess of those occurring at stagnation points.

On the other hand, SWBLI occurs, for instance, when the shock resulted from the SSI meets the launcher wall, thus promoting boundary layer separation and transition.

As a result, SSI and SWBLI demand accurate prediction for a reliable and affordable aero-thermal design of launcher vehicles.

In this framework, the results of the computational analysis of the flowfield past a double wedge test bed are reported and discussed in detail. This configuration, in fact, is a benchmark as it presents unique flow patterns typical of SSI and SWIBLI. In particular, the experiment of Swantek and Austin was selected and numerically rebuilt [9]. The test bed geometry is shown in **Figure 2**. It is a double wedge with $\theta_1 = 30^\circ$ and $\theta_2 = 55^\circ$ where the lengths of the first and second face are $L_1 = 50.8$ mm and $L_2 = 25.4$ mm, respectively.

Along with the center of the model 19 coaxial thermocouple gauges at 16 different streamwise locations are mounted. Therefore, several experimental data exist for numerical-to-experimental comparisons. The test campaign was performed by using high enthalpy air at the free-stream conditions summarized in **Table 1**.

The numerical rebuilding was carried out by means of a steady-state two-dimensional Reynolds-averaged Navier-Stokes (RANS) simulation performed with the commercial CFD tool Fluent. Air was modeled with a five species chemistry mixture (N_2, N, O_2, O, NO) in

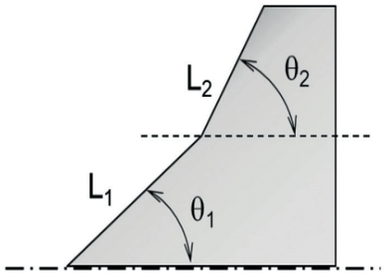

Figure 2. Test bed configuration with quotes.

Parameter	M7_8
Stagnation enthalpy (MJ/kg)	8.0
Mach	7.14
Static temperature (K)	710
Static pressure (kPa)	0.780
Velocity (m/s)	3812
Density (kg/m^3)	0.0038
Unit Reynolds number (10^6/m)	0.435

Table 1. Free-stream conditions of experiment.

thermo-chemical non-equilibrium conditions. Turbulence has been taken into account with the k−ω SST model. The wall was assumed isothermal (T_w = 298 K) and noncatalytic; while, in order to take into account the effects of the boundary layer transition, a trade-off analysis was undertaken (and not shown here for simplicity) in order to determine a proper flow transition location (x_{tr}) to fix along with the first ramp. Results highlighted that x_{tr} = 58% L_1 is a viable option. Further details about the numerical setting can be found in Ref. [10].

A structured multiblock mesh of 433 × 707 points was considered to solve for complex flow structure past the test bed. In particular, a great deal of care was taken in grid development. In fact, the distribution of grid points has been dictated by the level of resolution desired in various areas of the computational domain such as SSI, triple points, shear layer and recirculation region. An example of the computational grid is provided in **Figure 3**.

As far as numerical results are concerned, **Figure 4** shows the qualitative comparison between experimental data (i.e., Schlieren image) and the Mach isolines.

As one can see, CFD results compare rather well with the Schlieren. Indeed, the numerical flowfield presents the same structure as pointed out by the experimental data, as the triple point, due to a strong shock that originates ahead the recirculation bubble, the reattachment shock and the shear layer.

Results comparison in terms of pressure and heat flux distribution is presented in **Figure 5**, where measures available for the heat flux are also provided.

As shown, the computed heat transfer is within the experimental uncertainty upstream of the separation point at x_{tr} = 58% L_1 (i.e., x = 27 mm); while rather good agreement with experiment is observed over the second wall of the double wedge, where the heat flux and pressure overshoots take place due to the shear layer impingement.

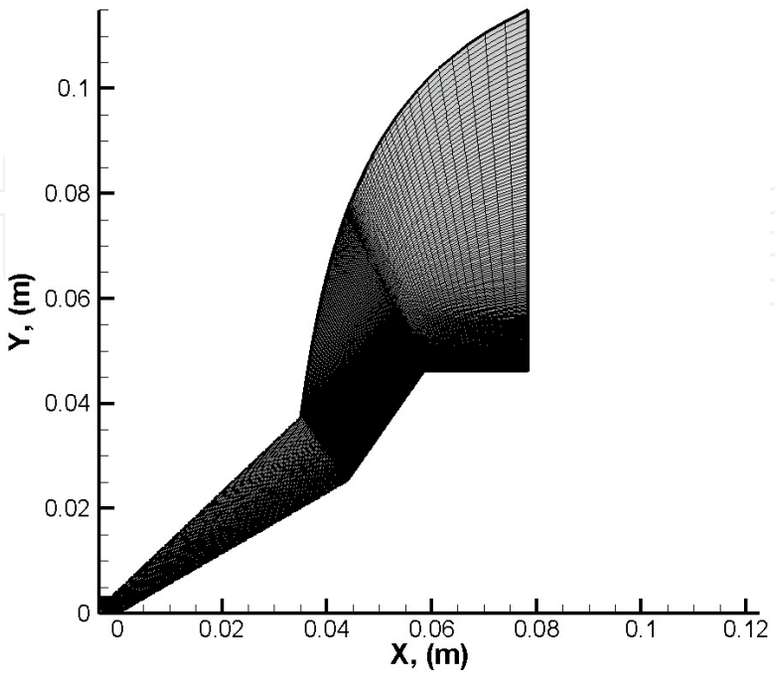

Figure 3. An example of the computational grid.

http://dx.doi.org/10.5772/intechopen.70757

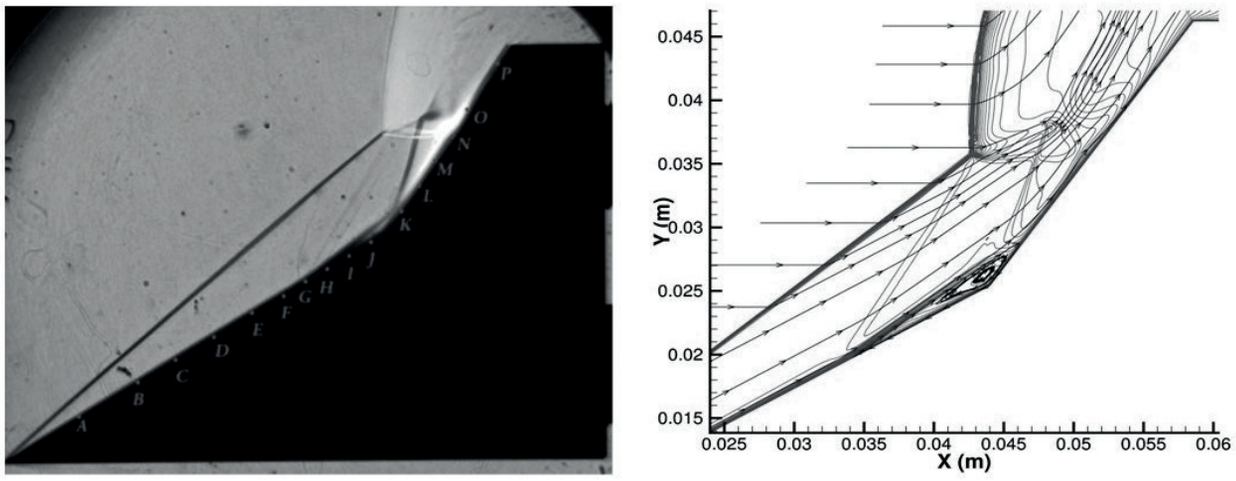

Figure 4. Comparison between Schlieren image and Mach isolines with streamtraces.

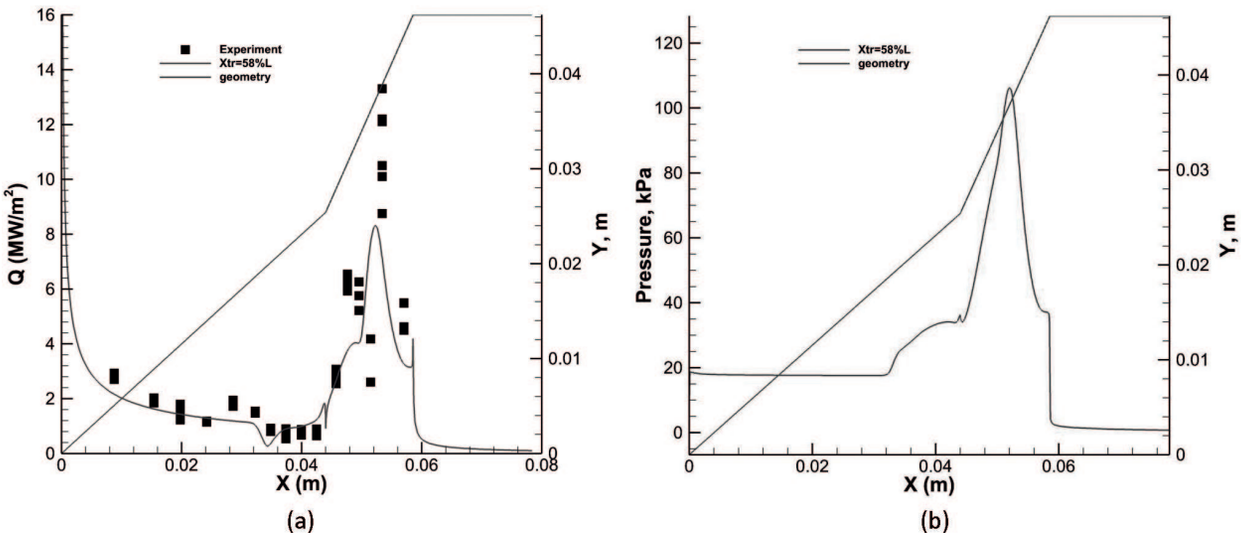

Figure 5. Heat flux and pressure profiles. Comparisons with experimental data.

In particular, **Figure 5** points out that CFD predicts well the recirculation bubble and the peak heat transfer location, but the numerical value is about 43% of that measured during the experiment [10].

Regarding pressure distribution, it is noticeable the pressure increase behind the separation shock on the first ramp. Then, a pressure overshoot, located just downstream of the reattachment point, is predicted on the second ramp. This is typical for the Edney type IV interaction. After the peak, the pressure suddenly drops toward the asymptotic pressure due to the strong expansion at the end of ramp [10].

3. Launcher aerodynamic appraisal

The launcher vehicle features a hummer head cylinder, as main body, with two boosters, see **Figure 6**. Non-dimensional aeroshape sizes are also reported in figure, being *L* the launcher

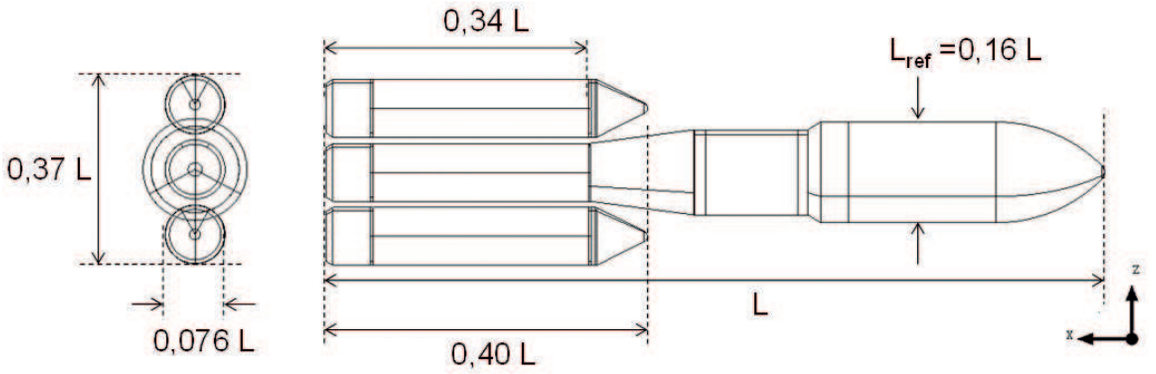

Figure 6. The launcher configuration.

height. As shown, the aeroshape under investigation also features a central core stage with a remarkable boat-tail configuration, which ends in correspondence of booster stage. The fairing diameter is 16% launcher height, while that of booster is equal to 0.076 L. The booster length is 40% of whole launcher's height [11].

Aerodynamic data for launcher are provided in the Body Reference Frame (BRF), as illustrated in **Figure 7** [11]. In this figure, aerodynamic force and moment coefficients are also provided, with sign convention according to the ISO norm. 1151.

The global aerodynamic force $\vec{F}$ and moment $\vec{M}$ acting on the launcher are expressed in BRF as follows:

$$\vec{F} = \left(-F_A\hat{i} + F_Y\hat{j} - F_N\hat{k}\right) = S_{ref}q_\infty\left(-C_A\hat{i} + C_Y\hat{j} - C_N\hat{k}\right) \tag{1}$$

$$\vec{M} = \left(M_l\hat{i} + M_m\hat{j} + M_n\hat{k}\right) = S_{ref}q_\infty L_{ref}\left(C_l\hat{i} + C_m\hat{j} + C_n\hat{k}\right) \tag{2}$$

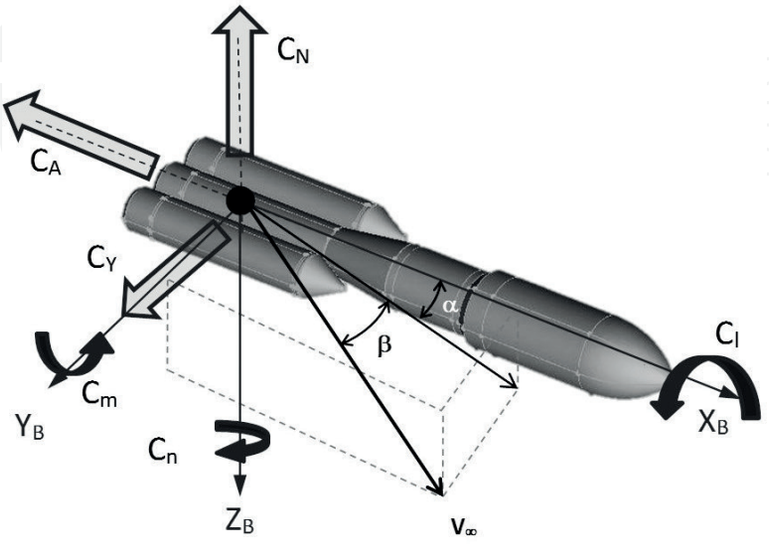

Figure 7. The body reference frame according to the ISO 1151.

where C_A is the axial force coefficient, C_Y the transverse force coefficient, C_N the normal force coefficient, $C_l = C_{Mx}$ the rolling moment coefficient, $C_m = C_{My}$ the pitching moment coefficient, $C_n = C_{Mz}$ the yawing moment coefficient, $\left(\hat{i}, \hat{j}, \hat{k}\right)$ are the reference unit vectors, S_{ref} the reference surface, L_{ref} the reference length (see **Figure 6**), and q_∞ the free-stream dynamic pressure.

The definition of force and moment coefficients is:

$$C_i = \frac{F_i}{S_{ref} q_\infty} \quad i = A, Y, N \tag{3}$$

$$C_i = \frac{M_i}{S_{ref} q_\infty L_{ref}} \quad i = l, m, n \tag{4}$$

where ρ_∞ is the atmospheric density and V_∞ the speed relative to air, and the reference quantities (see **Figure 6**) are:

$$L_{ref} = 0.16L \tag{5}$$

$$S_{ref} = \frac{\pi L_{ref}^2}{4} \tag{6}$$

The present preliminary assessment, however, focuses on the longitudinal aerodynamic only, i.e., C_A, C_N and C_m are addressed. Aerodynamic coefficients are important at system level for the assessment of launcher general loading determinations, performances and, as well as, control. For instance, performances studies use the axial force coefficient C_A since this aerodynamic force opposes to the vehicle movement. Further, the launcher control needs the evaluation of the aerodynamic moment at the CoG since the control software changes the rocket's thrust direction in order to null global incidence of the vehicle, except during maneuvers. Anyway, considering that propellants are constantly consumed along the ascent flight, the CoG location is continuously changing too. Therefore, it is preferred to provide aerodynamic moments at a conventional location, namely moment reference center (MRC), see **Figure 7**. The relationship for the pitching moment coefficient evaluation, passing from MRC to CoG, reads:

$$(C_m)_{CoG} = (C_m)_{MRC} + C_N \frac{\Delta x}{L_{ref}} - C_A \frac{\Delta z}{L_{ref}} \tag{7}$$

where $\Delta x = x_{CoG} - x_{MRC}$ and $\Delta z = z_{CoG} - z_{MRC}$ are evaluated in the Layout Reference Frame (LRF), as shown in **Figure 8**.

The flow regime investigated for launcher aerodynamic appraisal during ascent encompasses subsonic, transonic-supersonic and hypersonic regimes.

In the present research effort, the range $0.5 \leq M_\infty \leq 5$ is investigated. Indeed, launcher aerodynamics has been addressed considering four Mach numbers, namely 0.5, 1.1, 2.5, and 5, at three angle of attacks, i.e., $\alpha = 0$, 5, and 7°, as summarized by the CFD test matrix in **Table 2**. Therefore, Eulerian and Navier-Stokes 3D CFD computations have been carried out on several unstructured hybrid meshes and in motor-off (i.e., without the effect of rocket plume) conditions.

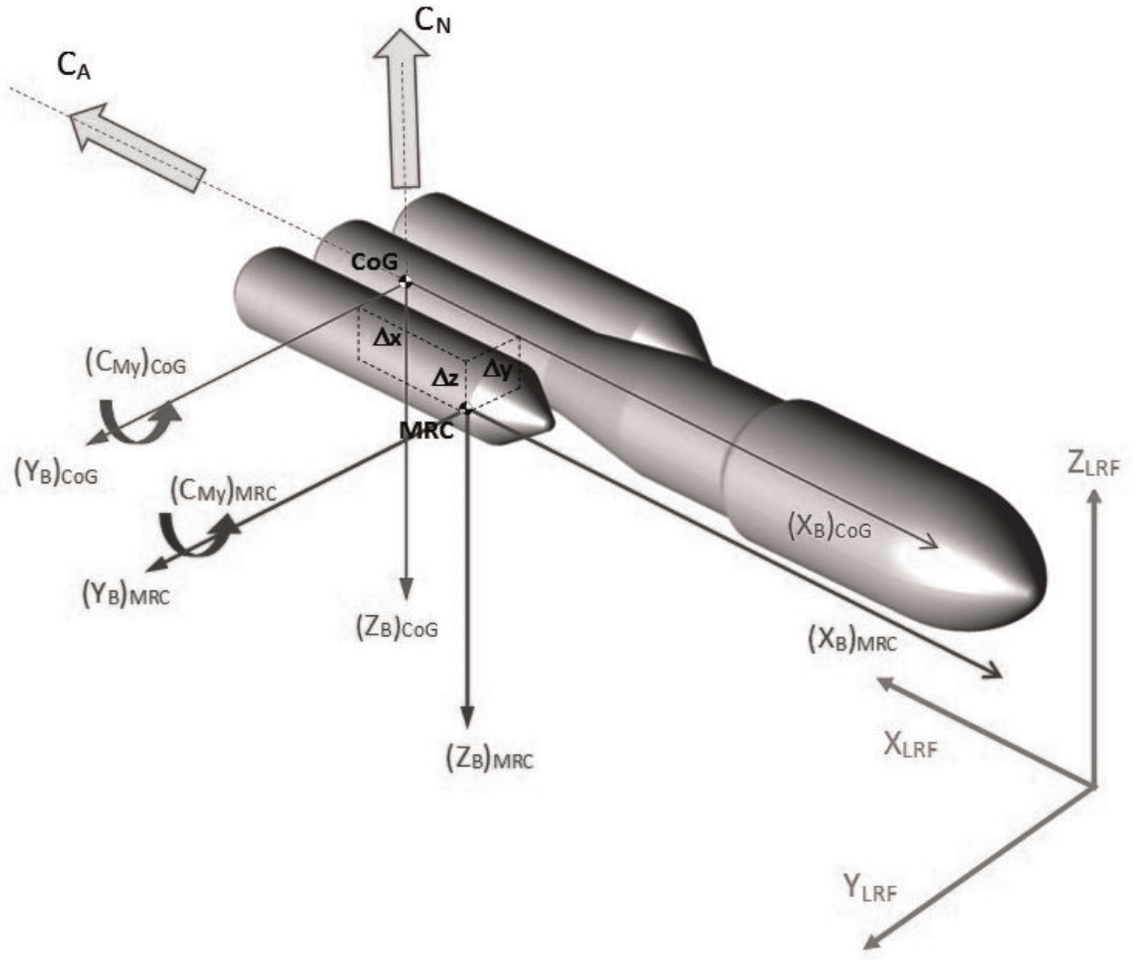

Figure 8. The layout reference frame.

α (°)	Mach			
	0.5	**1.1**	**2.5**	**5**
0	E	E	E	E
5	E	E	E, NS	E, NS
7	E	E	E	E

E: Eulerian CFD; NS: Navier-Stokes CFD.

Table 2. The CFD test matrix.

Engineering-based aerodynamic analyses were also performed by using a 3D Panel Method (PM) code, namely Surface Impact Method (SIM), developed by CIRA [12]. This tool is able to accomplish the supersonic and hypersonic aerodynamic and aerothermodynamic analyses of complex vehicles configuration by using simplified approaches as local surface inclination methods and approximate boundary-layer methods, respectively. Surface impact methods

http://dx.doi.org/10.5772/intechopen.70757

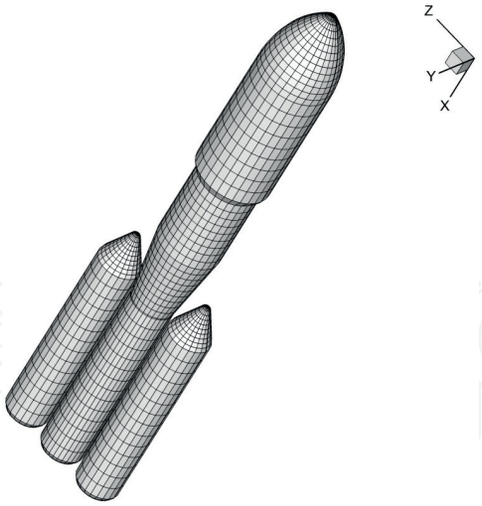

Figure 9. Panel code mesh for sup-hypersonic aerodynamics.

typical of Hypersonics, are Newtonian, Modified Newtonian, Tangent cone and Tangent Wedge theories [4].

A typical mesh surface that has been used for the engineering-level computations is shown in **Figure 9**. Some engineering-based aerodynamic results for axial and normal force coefficient are provided in both **Figures 17** and **19**, respectively.

On the other hand, the mesh domains for subsonic and sup-hypersonic speed flow simulations are shown in **Figures 10** and **11**, respectively [13].

As on can see, a square brick wide 20 body length upstream, downstream, upward and downward the launcher is considered to assure farfield unperturbed free-stream flow conditions at subsonic speed. Indeed, in this flow regime (i.e., elliptic flow), disturbances due to the

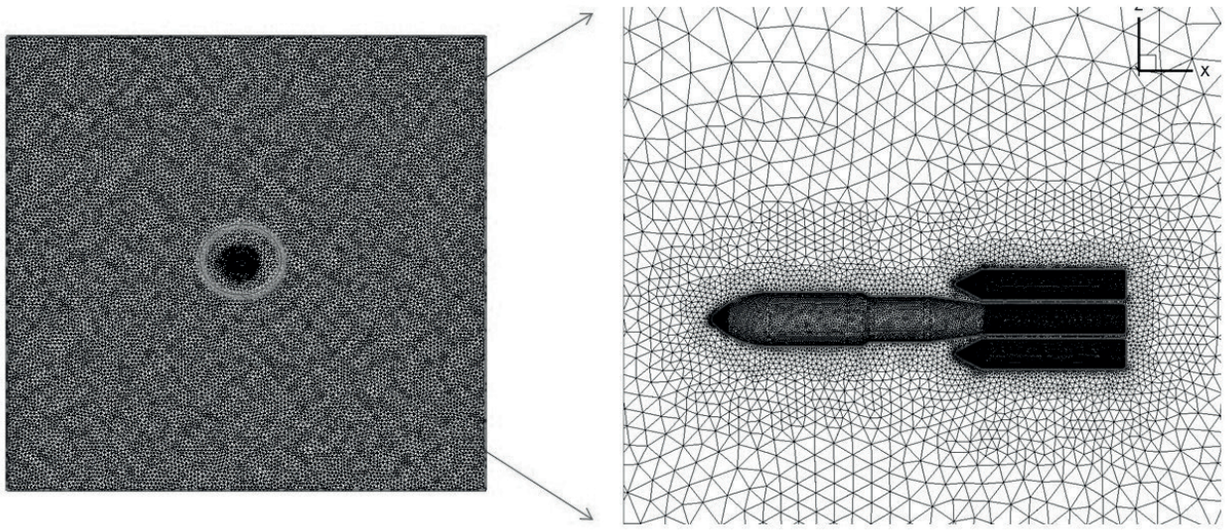

Figure 10. Overview of the hybrid mesh domain for subsonic speed.

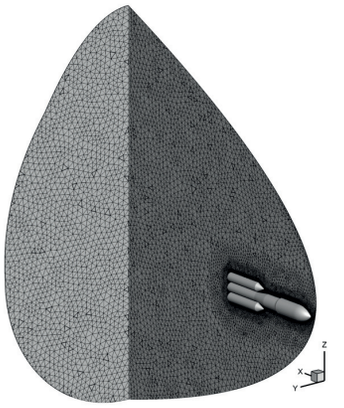

Figure 11. Overview of a hybrid mesh domain for sup-hypersonic CFD simulations.

body influence flow everywhere since they are propagated upstream via molecular collisions at approximately the speed of sound. Therefore, the computational domain must be wide enough to avoid interferences between flowfield and farfield boundary conditions.

At supersonic speed, however, a shock wave appears at launcher leading edge (i.e., hyperbolic flowfield) because of, when flow moves faster than the speed of sound, disturbances cannot work their way upstream but coalesce forming a standing wave, namely bow shock. As a result, the computational domain is quite narrow, as shown in **Figure 11**.

CFD results of the preliminary assessment of launcher aerodynamics are summarized from **Figures 12–21**. For instance, **Figure 12** shows the pressure distribution expected on the surface of the launcher flying at $M_\infty = 0.5$ and $\alpha = 5°$. Flow compression that takes place for this flight conditions at the stagnation regions of launcher fairings and of boosters' conical forebody is clearly shown. A recompression zone at the beginning of the cylindrical trunk, just after the fairings, and on that close to the boosters' forebody can be noted as well.

Results for numerical investigations at higher Mach numbers are provided in **Figure 13**. Here, an overview of pressure coefficient (Cp) distribution on launcher symmetry plane and surface is provided for $M_\infty = 2.5$ and $\alpha = 5°$.

Flow streamtraces on the symmetry plane are reported as well [13]. This CFD computation is carried out with SST k-ω turbulence flow model and for cold wall boundary condition (i.e., $T_w = 300$ K).

Results in **Figure 13** highlight a complex flowfield past the launcher due to the flow separation bubble at fairing boat-tail and the effect of fuselage/booster SSI and SWIBLI. For instance, after compression at conical flare of main fairings the flow undergoes to expansions that align it along with the constant cross section part of hammerhead. Hence, at the end of fairings another strong expansion takes place to accommodate the flow to the variation in launcher cross section (i.e., narrow cross section due to fairing boat-tail). Then, a shock wave arises at the beginning of the cylindrical trunk, just after the fairings, to redirect the flow along with the launcher wall.

Flow complexity increases further in the region close to the boosters leading edges, as also shown in **Figure 14**. This figure provides an overview of pressure coefficient distribution on launcher

http://dx.doi.org/10.5772/intechopen.70757

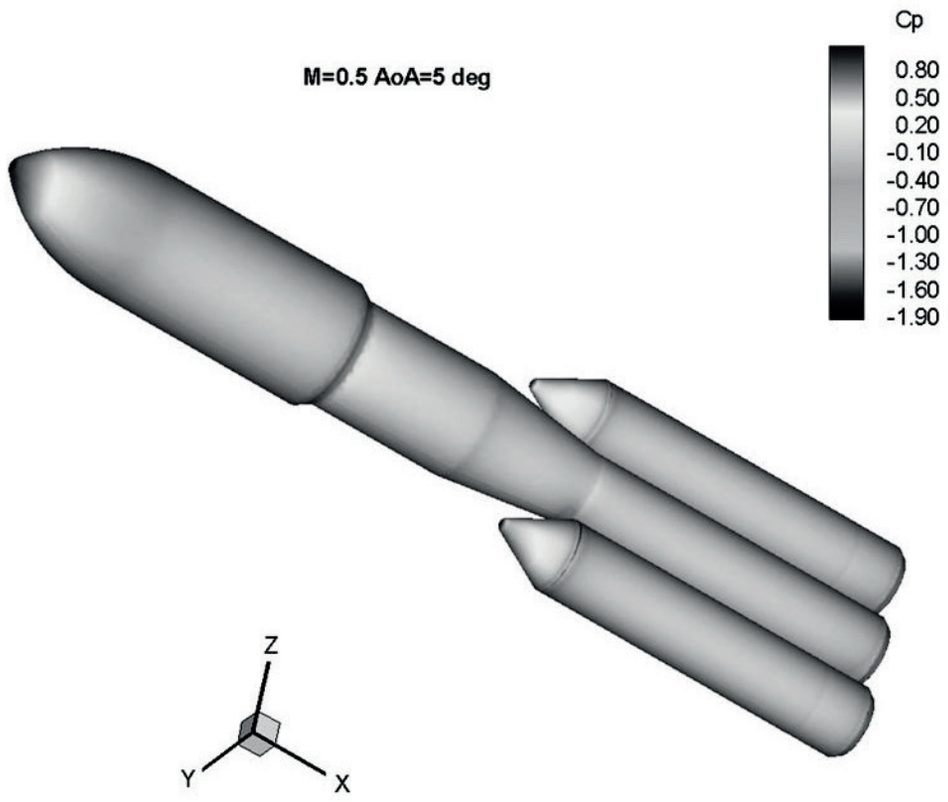

Figure 12. Pressure coefficient at $M_\infty = 0.5$ and $\alpha = 5°$.

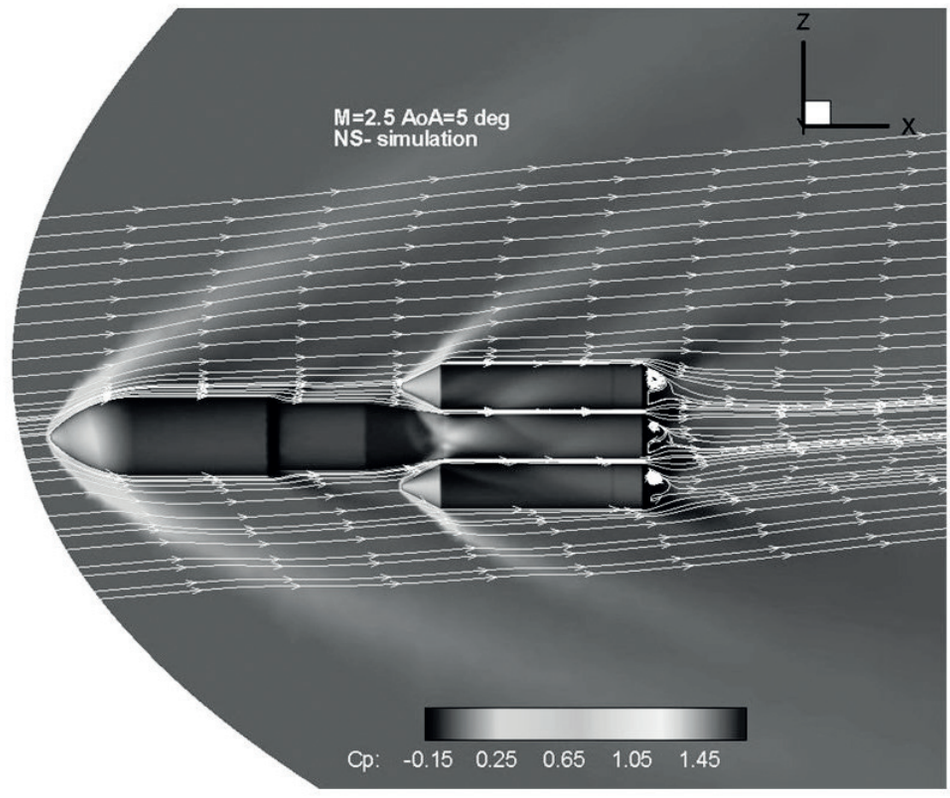

Figure 13. Overview of Cp distribution on symmetry plane and launcher at $M_\infty = 2.5$ and $\alpha = 5°$.

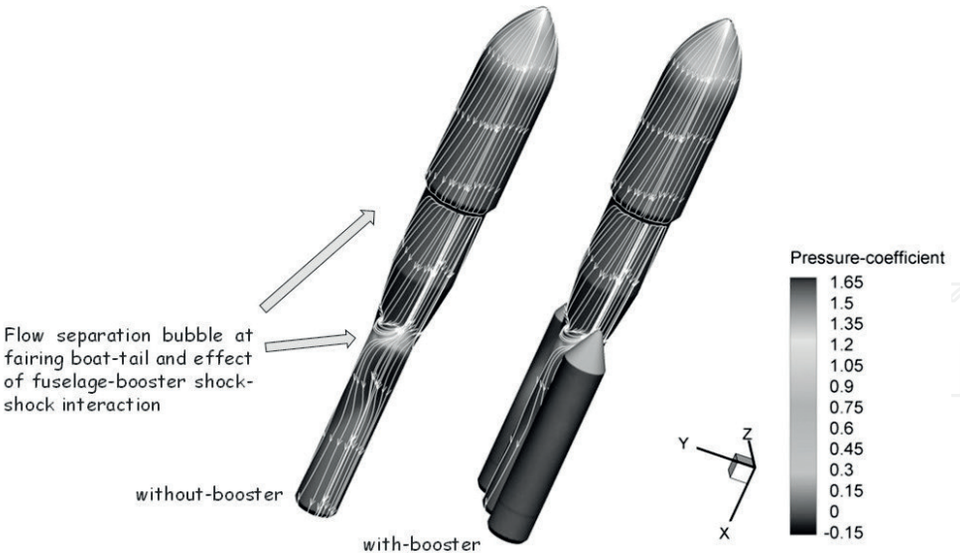

Figure 14. Contours of Cp with skin friction lines on launcher aeroshape at $M_\infty = 2.5$ and $\alpha = 5°$.

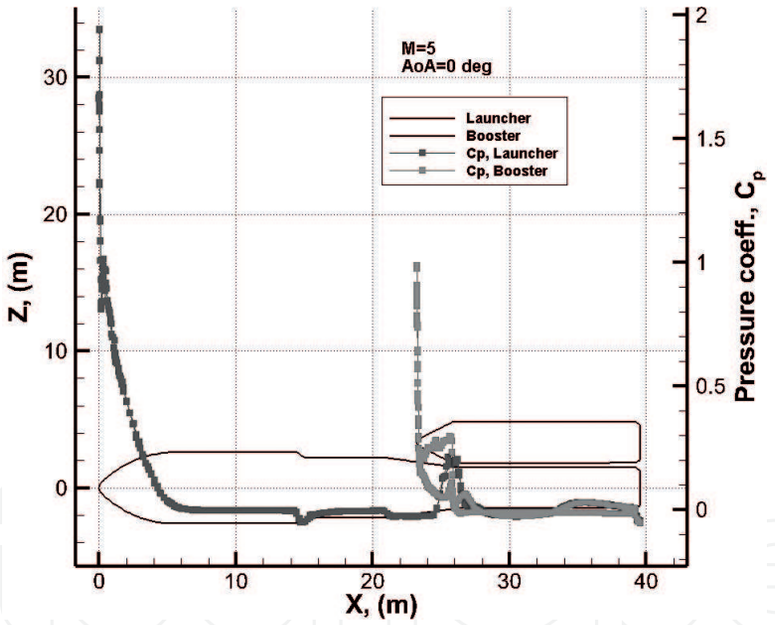

Figure 15. Profiles of Cp on launcher and booster centerlines at $M_\infty = 5$ and $\alpha = 0°$.

aeroshape with skin friction lines. As one can see, in the region close to the boosters' leading edges, complex SSI and SWIBLI phenomena take place. They result in higher thermo-mechanical loads (i.e., local pressure and thermal overshoots) on the launcher wall that must be carefully addressed in the vehicle design [13].

The effect of SSI between launcher and booster at $M_\infty = 5$ and $\alpha = 0°$ flight conditions is clearly highlighted by the pressure overshoots shown at about $x = 26$ m in **Figure 15**. As one can see, also at those flight conditions complex flowfield interaction phenomena are expected.

http://dx.doi.org/10.5772/intechopen.70757

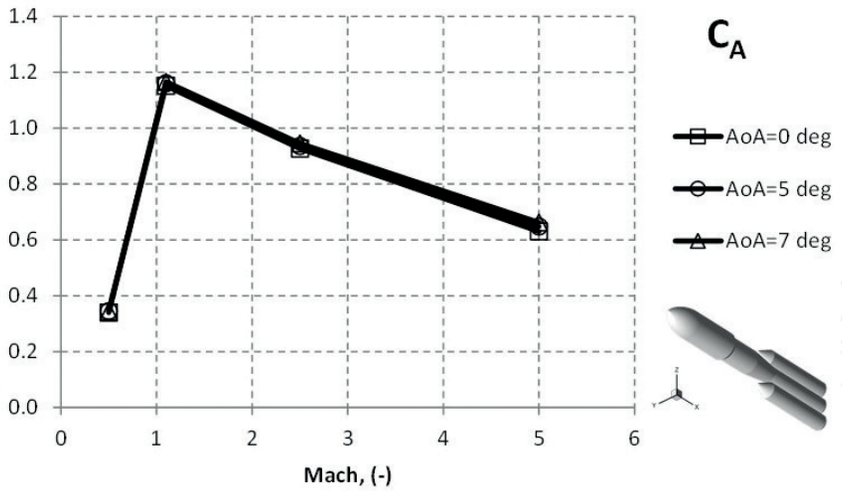

Figure 16. Axial force coefficient versus Mach at different AoA, namely α = 0, 5, and 7°.

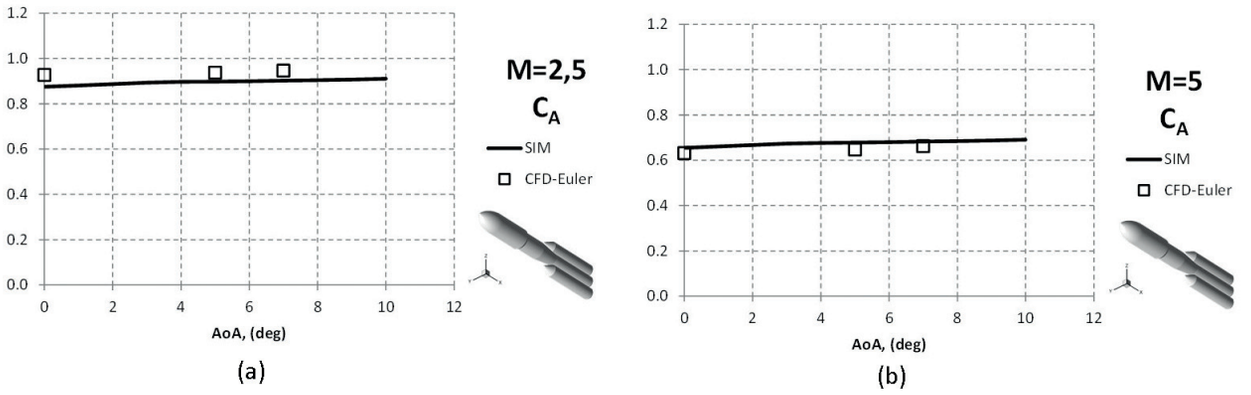

Figure 17. C_A versus AoA at M_∞ = 2.5 and 5. Comparison between PM and CFD results.

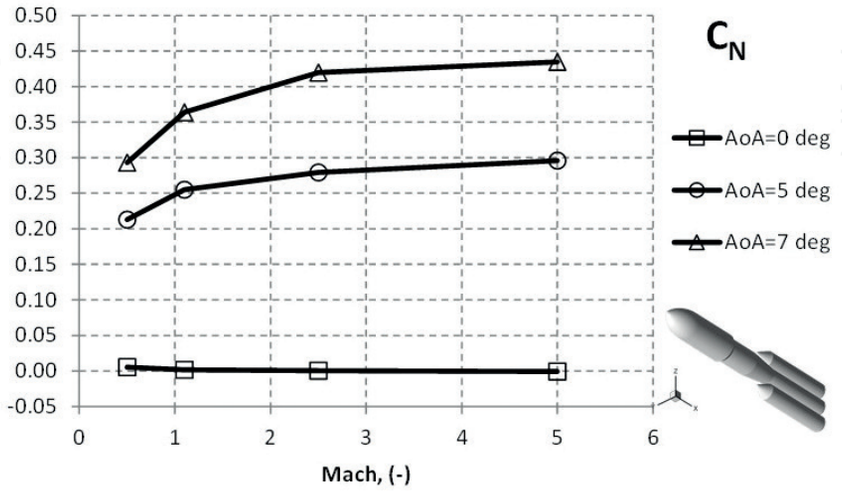

Figure 18. Normal force coefficient versus Mach at different AoA, namely α = 0, 5, and 7°.

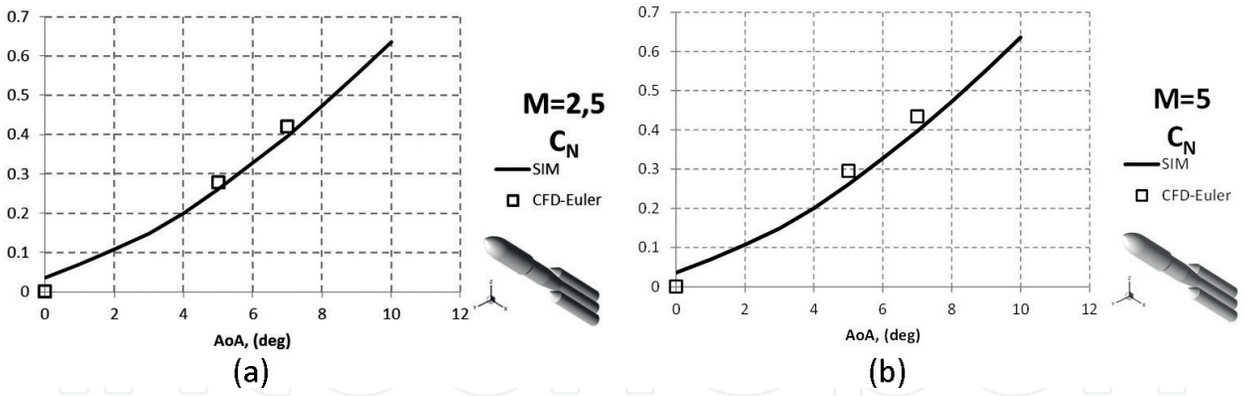

Figure 19. C_N versus AoA at M_∞ = 2.5 and 5. Comparison between PM and CFD results.

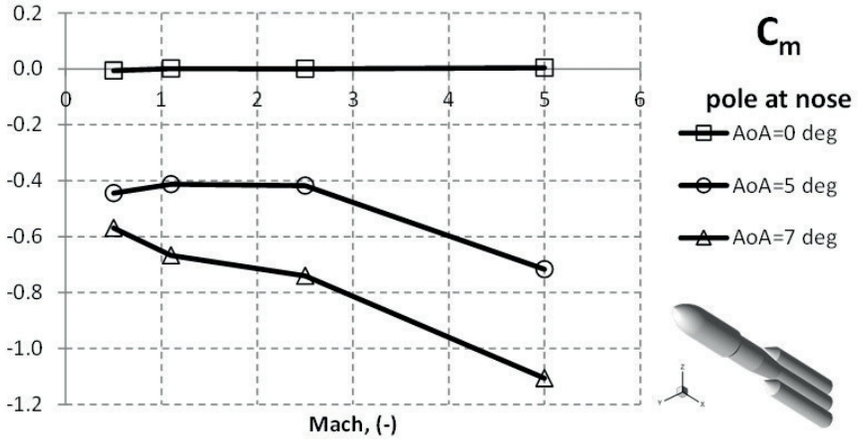

Figure 20. Pitching moment coefficient versus Mach at different AoA, namely α = 0, 5, and 7°.

As far as aerodynamic coefficients are concerned, results for launcher axial force, normal force and pitching moment coefficients are summarized from **Figures 16–21**. For instance, **Figure 16** shows the axial force coefficient versus Mach number at different AoA, namely α = 0, 5, and 7°. As one can see, C_A does not significantly change passing from 0 to 7° AoA at each considered Mach number.

On the contrary, the effect of flow compressibility is remarkable, as expected. Indeed, the strong increase to which undergoes the axial aerodynamic force, when M_∞ becomes transonic, is due to the wave drag contribution, as expected. Nevertheless, this contribution tends to be less strong as Mach number goes toward hypersonic speed conditions considering that the shock becomes weak due to the streamlined vehicle aeroshape (i.e., high inclined shock to assure a narrow shock layer).

The variation of C_A versus the angle of attack, α, at M_∞ = 2.5 and 5 is provided in **Figure 17**, where a comparison between SIM and CFD results is also available. As shown, engineering and numerical results compare rather well, thus confirming the reliability of the panel methods outcomes [14].

Regarding normal force coefficient results, **Figure 18** highlights that, for each Mach number, C_N features a quite linear slope as α increases up to 7° AoA. In addition, in this case,

http://dx.doi.org/10.5772/intechopen.70757

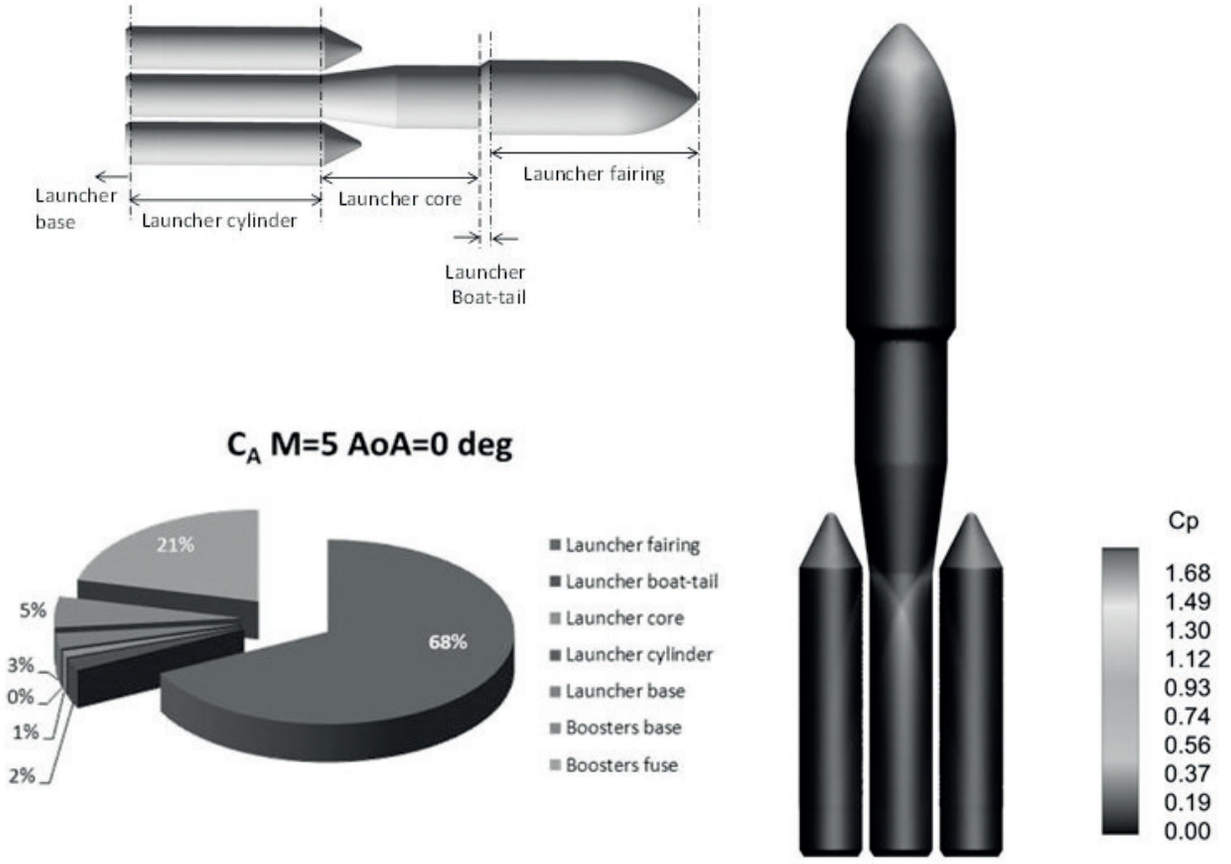

Figure 21. C_A breakdown at $M_\infty = 5$ and $\alpha = 0°$.

compressibility effect influences launcher normal force by means of different curve slopes for each Mach number. Results comparison between SIM and CFD is provided in **Figure 19** at $M_\infty = 2.5$ and 5.

As one can see, the reliability of the panel methods outcomes is still confirmed.

The vehicle pitching moment coefficient features a behavior quite close to that described for the C_N, but with a strong pitch down detected moving toward $M_\infty = 5$.

Note that both C_N and C_m at $\alpha = 0°$ are null due to the symmetric launcher aeroshape.

Finally, the axial coefficient breakdown at $M_\infty = 5$ and $\alpha = 0°$ is shown in **Figure 21**. Here the lumped contributions of launcher fairings, boat-tail, core, cylinder, and base, as well as of booster fuse and base are recognized. As one can see, launcher fairings contribute to about 68% of total drag coefficient; while this percentage for booster fuselage and base is close to 21 and 5%, respectively.

4. Conclusion

In this research effort launcher aerodynamic design activities at phase-A level are described.

The goal is to address the preliminary aerodynamic database of a typical launch vehicle configuration as input for performances evaluations as well as launcher control, sizing, and

staging dynamics. To this end, both reliable engineering-based and steady-state computational fluid dynamics, with both Euler and Navier-Stokes approximations, are carried out at several Mach numbers, vehicle attitude conditions, and in motor-off conditions. In particular, launcher aerodynamic performance is provided in terms of axial, normal and pitching moment coefficients. Numerical results point out that the axial force coefficient does not significantly change passing from 0 to 7° angle of attack at each considered Mach number; while the effect of flow compressibility is remarkable. Regarding normal force coefficient, results highlight that, for each Mach number, it features a quite linear slope as the angle of attack increases up to 7°. Finally, the behavior of the vehicle pitching moment coefficient is quite close to that described for the normal force coefficient, but a strong pitch down is detected when launcher speed becomes hypersonic.

Author details

Giuseppe Pezzella[1]* and Antonio Viviani[2]

*Address all correspondence to: g.pezzella@cira.it

1 Italian Aerospace Research Centre (CIRA), Capua, Italy

2 University of Campania "L. Vanvitelli", Aversa, Italy

References

[1] Pallegoix JF. Launcher Aerodynamics. NATO: STO-EN-AVT-206; 2014

[2] Viviani A, Pezzella G. Next Generation Launchers Aerodynamics, T.C. 37/661 (2). Fort P. O., Trivandrum-695 023, Kerala, India: Research Signpost; 2012. ISBN: 978-81-308-0512-2

[3] Catalano P, Marini M, Nicolì A, Pizzicaroli A. CFD contribution to the aerodynamic data set of the Vega launcher. Journal of Spacecraft and Rockets. 2007;**44**(1):42-51 http://dx.doi.org/10.2514/1.23534

[4] Bertin JJ. Hypersonic Aerothermodynamics. AIAA (American Institute of Aeronautics and Astronautics). Washington; 1994

[5] Anderson JD. Hypersonic and High Temperature Gas Dynamics. New York: McGraw-Hill Book Company; 1989

[6] Rogers SE, Dalle DJ, Chan WM. CFD simulations of the space launch system ascent aerodynamics and booster separation. In: 53rd AIAA Aerospace Sciences Meeting, AIAA SciTech Forum, (AIAA 2015-0778) https://doi.org/10.2514/6.2015-077

[7] Viviani A, Pezzella G. Computational flowfield analysis of a next generation launcher. In: 6th European Conference for Aeronautics and Space Sciences (Eucass); 29 June-3 July 2015; Krakow, Poland

[8] Pezzella G, Marini M, Roncioni P, Kauffmann J, Tomatis C. Preliminary design of vertical takeoff hopper concept of future launchers preparatory program. Journal of Spacecraft and Rockets. 2009;**46**(4):788-799. DOI: 10.2514/1.39193 ISSN: 0022-4650

[9] Swantek AB, Austin JM. Heat transfer on a double wedge geometry in hypervelocity air and nitrogen flows. In: 50th AIAA Aerospace Sciences Meeting including the New Horizons Forum and Aerospace Exposition; 09–12 Jan 2012; Nashville, Tennessee. AIAA 2012-0284

[10] Knight D, Chazot O, Austin J, Ali Badr M, Candler G, Celik B, de Rosa D, Donelli R, Komives J, Lani A, Levin D, Nompelis I, Panesi M, Pezzella G, Reimann B, Tumuklu O, Yuceil K. Assessment of predictive capabilities for aerodynamic heating in hypersonic flow. Progress in Aerospace Sciences. 2017;**90**:39-53 http://dx.doi.org/10.1016/j.paerosci.2017.02.001

[11] Viviani A, Pezzella G. Numerical analysis of the flowfield past a next generation launcher. In: 20th AIAA Hypersonics. Strathclyde University Technology & Innovation Center; 6-9 July 2015; Glasgow, Scotland. AIAA-2015-3535. DOI: 10.2514/6.2015-3644

[12] Pezzella G. Preliminary aerodynamic and aerothermodynamic assessment of the VTO Hopper booster. ISRN Mechanical Engineering. 2011;**2011**:15. Article ID 215785. DOI: 10.5402/2011/215785

[13] Viviani A, Pezzella G, D'Amato E. Aerodynamic analysis with separation dynamics of a launcher at staging conditions. In: 30th Congress of International Council of the Aeronautical Sciences. ICAS 2016. DDC Daejeon Korea; September 25-30, 2016

[14] Pezzella G. Aerodynamic and aerothermodynamic design of future launchers preparatory program concepts. Aerospace Science and Technology. December 2012;**23**(1):233-249 http://dx.doi.org/10.1016/j.ast.2011.07.011

IntechOpen